Chapter 9
Field Case

Dynamic hazards predicting can be divided into single-stage predicting and large-scale mining predicting. China's metal mine production is relatively backward, a wide range of workplaces are not suitable for portable instruments into the stope for one-on-one monitoring and predicting. In addition, the monitoring results of single stope can not reflect the trend of large-scale hazard. Large-scale mining area and continuous mining area of hazard monitoring and predicting should take multi-channel instrument for positioning processing dynamic hazard (Cheng et al. 2006; Liu 2008; Li et al. 2005).

It is difficult to explain the dynamic hazards with traditional rock mechanics theory. People attempt to use the microseismic monitoring technology to predict dynamic hazard. For a long time, despite the precursor features and anomalies do not always indicate the advent of hazards. Compared with the traditional rock mechanics method, the predicting system must have a fundamental innovation in theory. In this chapter, based on the non-deterministic theory, which includes the mutation theory, synergetics, dissipative theory, fractal structure theory and artificial neural network system, the demonstration model for mine dynamic hazard monitoring was established. All of these monitoring includes: microseismic monitoring, predicting criteria models and synergetic monitoring methods. These field cases verified that these proposed aforementioned theoried and methods can predict rockburst in a reliable mode; these are meaning discoveries for predicting rockburst.

9.1 Design of Microseismic Monitoring System in Huize Lead-Zine Mine

In order to predict the mine dynamic hazard, microseismic monitoring technology has become the main method to realize the predicting of dynamic hazard in deep mining. The geophones can be used to detect the elastic wave emitted by the rupture

C. Wang, *Evolution, Monitoring and Predicting Models of Rockburst*,
https://doi.org/10.1007/978-981-10-7548-3_9

source of rockmass using the microseismic monitoring system. The waveform can determine the coordinates and intensity of microseismic activity. Based on microseismic monitoring technology, we can get the potential micro-earthquake activity criterion and achieve predicting by micro-rupture information. Microseismic monitoring is widely used to predict the dynamic hazards in deep mining.

9.1.1 Main Influence Factor

Due to the particularity of deep mining, it can not rely solely on the theory to optimize the design of microseismic monitoring system. At the scene, we selected the initial selection of basic monitoring according to the mining project development and quasi-engineering layout. Then, we optimized the position of sensor within the scope of monitoring, the monitoring of target was ensured to meet the requirements and the monitoring range to the maximum.

In general, the establishment of a microseismic monitoring system must consider the following factors:

1. Monitoring object;
2. Monitoring range;
3. The objective environment of the object to be monitored;
4. Monitor the goals to be achieved;
5. Investment in monitoring systems;
6. Positioning accuracy.

In order to achieve the purpose of optimization program, we need fully consider the above factors, the design was optimized.

9.1.2 Microseismic Monitoring System

As shown in Fig. 2.7, the monitoring system consists of surface monitoring station, underground data exchange center (EQ), signal acquisition sensor (QS) and sensors. Due to the limitations of underground environment conditions, the layout of underground data exchange center should be considered:

(1) Choose a quiet location away from the mining area;
(2) Closing to the sensor and reducing the overall length of communication cable;
(3) Builting in a more stable rock formation to ensure the safety of data exchange center;
(4) Consider the use of underground power supply to facilitate communication with the surface monitoring station;

(5) Consider underground ventilation, moisture and other environmental problems;
(6) Easy to transport cables and cable laying.

This microseismic monitoring system was divided into two parts: the surface and the underground parts, they were the long-term monitoring service facilities.

9.1.3 Sensor Arrangement Design

Regarding on the installation of microseismic monitoring system, the preliminary consideration: Considering the orebody occurrence conditions, mining methods and existing engineering layout, a QS system was be layout 1451 m level, two sets of QS was arranged in 1391 m level, a QS system was in 1331 m level, as shown in Fig. 2.7.

9.2 Case Verification

Microseismic signals contain large amounts of information. Through the analysis of precursory characteristics of microseismic signals, dynamic hazard can be predicted using these parameters.

9.2.1 Predicting Case Based on Displacement Nephogram

The displacement change of microseismic events varies with different periods during excavation. Many periods increase suddenly, while in some cases the increase rate is smaller, and the overall pattern is unbalanced. The cumulative displacement curves show that rock failure status. When it suddenly increases greatly, it indicates the rock failure. The phenomenon can be used as the precursor information characteristic of rock failure, which is usually formed by the accumulation of stress and deformation of rockmass. However, due to the frequent mining field blasting, drilling excavation, especially when underground mining activity is not stable, and the structure of underground mining goaf due to mining activities suddenly produce large changes, accumulation of microseismic parameters also will produce a sudden change. These changes often rebalance over a period of time, microseismic events will decrease and their strength will decrease. Therefore, when the change pattern of microseismic events is predicted by displacement accumulation curve, the underground mining activities are combined to reflect the actual situation.

As shown in Fig. 9.2, microseismic monitoring data was from April 14th, 2009 to 30th, it showed that the distribution characteristics of microseismic events using microseismic monitoring system XQuery software.

The gradual extraction of orebody was shown in Fig. 9.1, Activity distribution of induced microseismic events were activity in 6 layers and two plates in the middle section of 1391 m in April 2009, The red line represents the exploration line and typical fault distribution, the orebodies were included in the blue line frame as indicated by the key monitoring areas. The intermediate microseismic monitoring events indicated the displacement characteristics of rockmass, and the color ranges from light blue to red indicated displacement, microseismic events of different colors indicated the development process of rock displacement induced by microseismic events.

As shown in the displacement nephogram of Fig. 9.1, it could be found that the rockmass displacement was mainly between the 52 lines and the 54 lines, and there was a trend of development near the fault. Based on the microseismic monitoring data, it showed that the development of rockmass displacement was mainly concentrated near the fault. The stope No. 3, which was in the middle two layered panel of 1391 m, produced a larger displacement in the vicinity of line 52 (red circle) 4.57E−4 m. With the development of mining, the displacement increased gradually to 4.92E−4 m, the change was small, but the range of deformation increased, especially in front of fault.

Through the displacement of microseismic events was analyzed and compared in different mining area, it could draw the displacement range and development trend occurred in a certain period of time of microseismic events, and obtained the risk of dynamic hazard caused by mining.

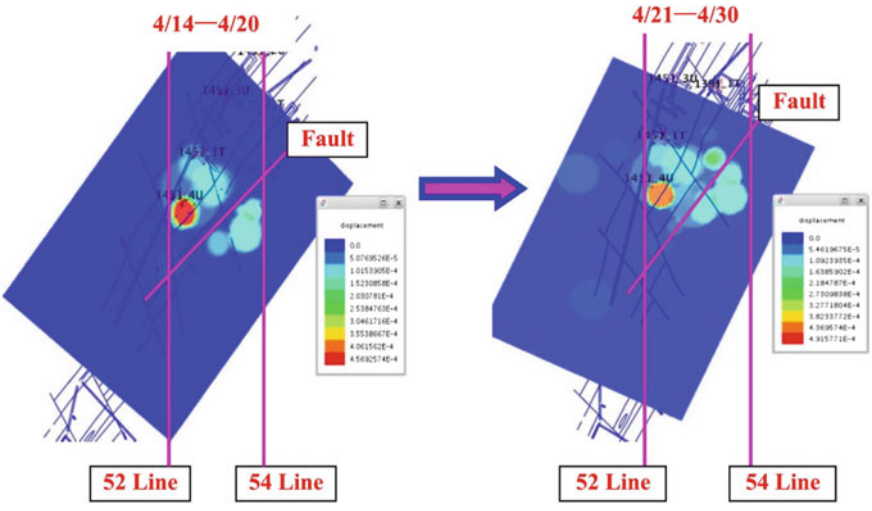

Fig. 9.1 Displacement nephogram

9.2.2 Predicting Case Based on Apparent Stress

Because mining disturbed the stress status of original rock, microseismic events were caused by rockmass failure, shear stress. Before the failure of rockmass, shear stress showed the stress drop of hypocenter. According to quantitative seismology theory, stress level and stress drop $\Delta\sigma$ of earthquake source rock could be expressed by seismic apparent stress σ_A. The deformation produced by earthquake source failure could be expressed by displacement $X(x, y, z)$. Therefore, it was known that stress-strain status of rockmass could be obtained by the spatial location, occurrence time t, focal sight stress σ_A and displacement u of microseismic events. That is to say, in a certain period of time Δt and space volume ΔV of rockmass, microseismic events could be used to describe the spatial distribution of stress and deformation in rockmass.

According to the existing condition of 8# ore body and the characteristics of mining engineering layout, the stress distribution at different elevation levels can provide a simple and direct description of microseismic activity in the mining area, a series of apparent stress distributions at different time periods were plotted in the visual stress analysis diagram. As shown in Fig. 9.2, many colors represented the apparent stress status at different times. The maximum apparent stress was 4.93 Pa in the fault position. With the recovery, the central region was not through the two segment stress and apparent stress, but stress concentration area in the near fault. As the right view is showed, the stress concentration area was also expanding, but the apparent stress value changed little. The occurrence, concentration, development and coalescence of apparent stress showed that large scale mining engineering caused obvious stress concentration or deformation concentration. Therefore, with

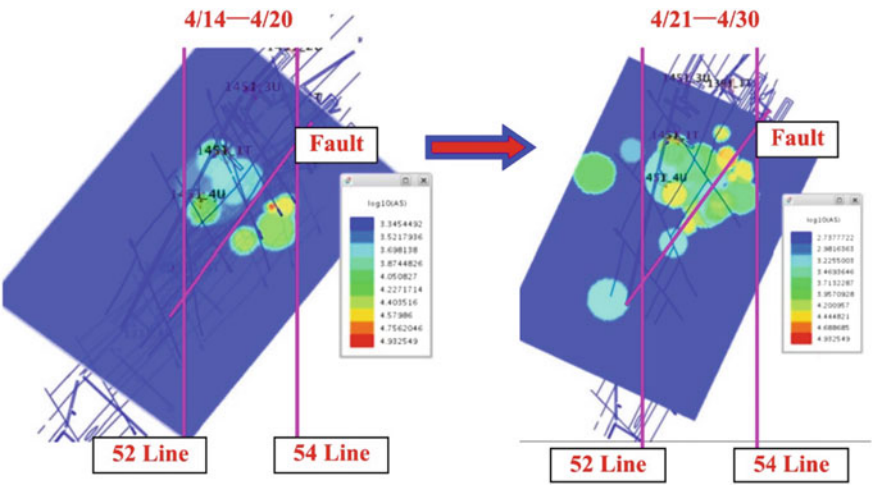

Fig. 9.2 Visual stress variation nephogram of microseismic monitoring events

the development of mining, using the development trend of apparent stress of rockmass, monitoring can be strengthened in this area to ensure safe production.

9.3 Predicting Key Points Identification of Dynamic Hazard

9.3.1 Dynamic Hazard Predicting Using Routine Monitoring

A case to verify the method of Tangent Modulus (TM) identification of dynamic hazard predicting critical point, which changes after the point *B* tangent modulus to determine the damage degree of rock deformation, so as to identify the key points to realize dynamic hazard predicting.

It is a very important method to obtain reliable physical parameters of rockmass using field monitoring instrument. According to the field engineering environment and mining plan, the stress and displacement monitoring, which was in 8# ore body 1331, 1345, 1369 and 1391 m, were carried out in four stages, and the 1369 m monitoring data were selected to be analysis. The surrounding rockmass was C_{1b}, and multi-point displacement meter were installed to monitor the displacement change in 1369-1 and 1369-4 bore holes; a bore hole stress gauge was installed in bore holes 1369-2, 1369-3 and 1369-9, the change of maximum principal stress was used to monitor in 1369-3 (the direction of ore body), and the tendency of stress changes was monitored in 1369-9 along with the direction of orebody; multi-point displacement meter was equipped with drilling 1369-7 and 1369-8 to monitor the deformation of rockmass caused by the minimum principal stress.

Through the stress and deformation of 1369 m segment rock was monitored, it was shown that the stress increment was only 1.2 MPa. With the gradual progress of mining engineering, the stress increased gradually, and the increase of displacement was unconspicuous in a long time. As shown in Fig. 9.3, until the point *B* in the elastic stage, TM remained nearly straight up, reached at 1, 243 MPa, the stress increment caused by the energy accumulation increased gradually the inner rockmass. As shown in Fig. 9.4, stress increment value increased slowly after the point B, the displacement changed greatly, TM decreased rapidly, and the change tended to be gradual only 880 MPa. It showed that rockmass passed through the yielding point, and rockmass was gradually developing to the instability direction. Until the failure, the average modulus of rock was 610 MPa. Therefore, the *B* point was defined as a predicting point. From the apparent observation of rockmass, micro-cracks expanded and failure, energy was released, the bearing capacity of rockmass decreased gradually, and the failure strain rate further speeded up. The instrument could not be monitored because of local damage in October 28th, 2010. In conclusion, it was reasonable to take yield point *B* as a key predicting

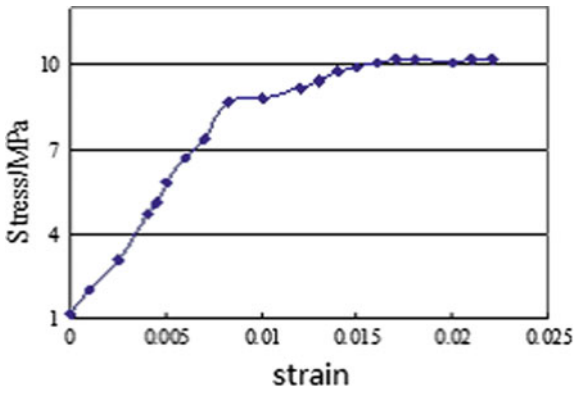

Fig. 9.3 1369 m stress strain curve. From Wang (2013)

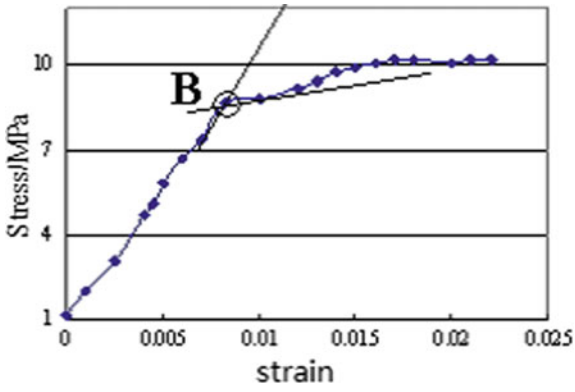

Fig. 9.4 Identification of predicting key points based on TM. From Wang (2013)

point. If the stress passed through the yield point *B*, but the stress may increased slowly and the deformation slowed down. Therefore, rockmass would have a long time to reach the peak strength, and then the rockmass would be failure. TM at the peak strength was 0, TM divided into several segments which was the yield point to the peak intensity for predicting rock failure.

9.3.2 Predicting Key Point Identification Using CAV and MS Events Activity

MS activity rate and Cumulative apparent volume (CAV) of low-energy and small-magnitude MS events had sharply increased, as shown in Fig. 9.5. When the high-energy and high-magnitude MS events increased dramatically, rockmass had passed through the elastic stage and began to enter the yield point (12 h 00 until 24 h 00 on September 10th, 2009). The MS events activity rate peaked between

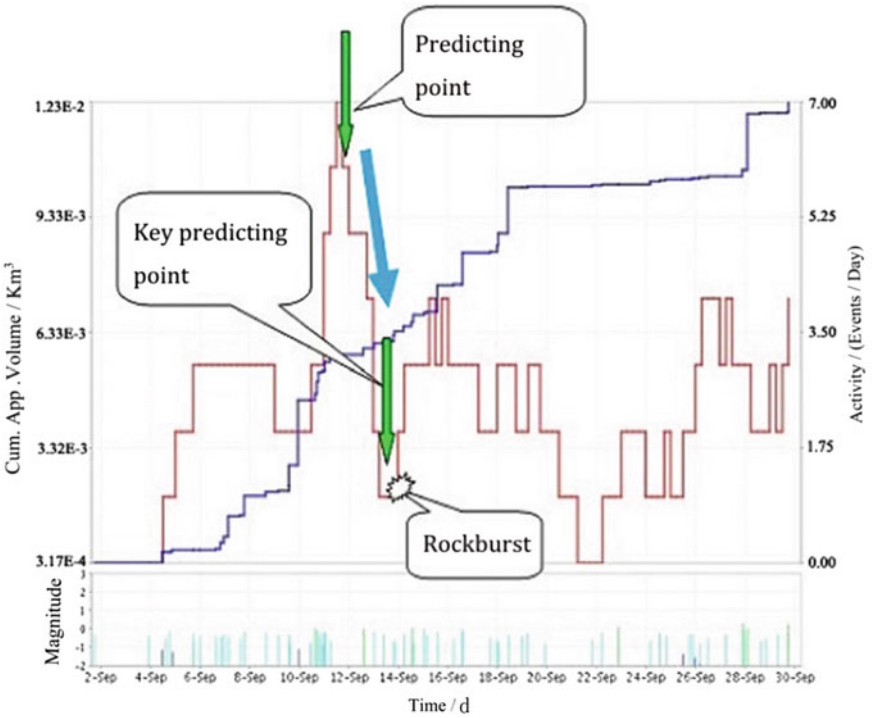

Fig. 9.5 Indentifying the predicting key point with microseismic events activity rate and CAV. After Wang (2014)

14 h 00 and 18 h 00 on September 11st, 2009 and then rapidly declined. This chapter defined the predicting point of rock failure as from 22 h 00 until 24 h 00 on September 11st, 2009. When MS events entered a relatively quiet period accompanied by a CAV surge from 0 h 00 until 4 h 00 on September 13rd, 2009, this point was interpreted as a key predicting point. At 0 h 00 on September 14th, 2009, roadway collapse accidents occurred in mine road 2, slice 6, sublevel 1369, level 1331 m (argillaceous limestone, approximately 100 t), and the activity rate of MS events and CAV of seismic source simultaneously increased sharply, as shown in Fig. 9.5. Rock failure was located with MS monitoring system in Fig. 9.6, and occurred in field in Fig. 9.7. The results showed that stress entered the predicting point of rockburst with the sharp increase in the activity of MS events and CAV. With increasing stress, the beginning of quiet period of MS events was the predicting key point of rockburst. After the quiet period, MS events were active and CAV increased sharply, rockburst occurred.

It should be noted that the relationship between rockmass failure and a decrease in MS event activity rate or increase in the CAV was an unnecessary but sufficient condition. The decreased AE events might be the stage of original crack compaction, so rockburst might not occur after predicting. Therefore, not all decreased

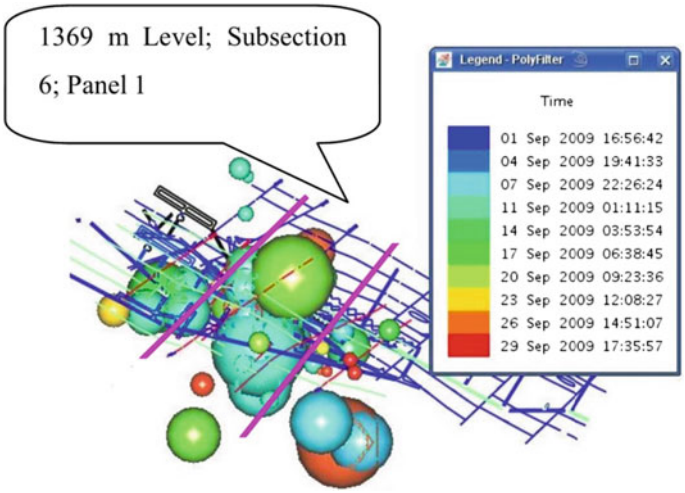

Fig. 9.6 Distribution of microseismic events. From Wang (2014)

Fig. 9.7 Collapse in 2# tunnel. With kind permission from "PERGAMON-ELSEVIER SCIENCE LTD": Fig. 5, Wang (2014). All rights reserved

in MS events activities or increased in the CAV indicated that rockmass was about to incur inevitable instability. However, it could play a key role in predicting rockburst. In the field, MS monitoring was using to predict rockburst in deep mining. Advanced monitoring was implemented by MS throughout the entire process of rockmass deformation. The activity rate and CAV of low-energy and small-magnitude MS events had sharply increased, as shown in Fig. 9.5. Rockburst was located with MS monitoring system in Fig. 9.6, and occurred in field in Fig. 9.7. The results showed that stress entered the predicting point of rockmass instability with the sharp increasement in the activity of MS events and CAV. With increasing stress, the beginning of quiet period of MS events was the predicting key point of rockburst. After the quiet period, MS events were active and CAV increased sharply, rockburst occurred.

9.4 Predicting Model of Rockburst Based on Bayesian Theory

9.4.1 Training Samples

We have been engaged in field tests and laboratory research on underground engineering dynamic hazard prevention for 16 years. It was determined that rockburst grades are approximately power-law distribution. That is, strong and very weak rockbursts are relatively less frequent, while moderate and weak rockbursts account for the majority of cases. The Bayesian discriminant model is based on assuming a normal distribution for the input variables, as well. The geological description, in situ stress measurement, and laboratory testing procedures were described previously. Experimental samples were randomly selected from a large data set for training the Bayesian model. The basic parameters of training samples and associated rockburst grades are listed in Table 9.1.

9.4.2 Predicting Rockburst Tendency Using a Bayesian Model

In this chapter, the critical factors, such as $R_b(X_1)$, $R_\theta(X_2)$ and $W_{\text{et}}(X_3)$, were used as the basic parameters for predicting rockburst risk using a Bayesian model.

Table 9.1 Critical factors of training samples

No.	σ_c	σ_t	σ_θ	R_b	R_θ	W_{et}	Actual rockburst grades
1	100.08	8.46	60.70	11.83	0.61	6.56	Strong
2	140.68	10.89	78.40	12.92	0.56	5.52	Strong
3	250.54	9.85	97.55	25.44	0.39	8.60	Strong
4	88.77	3.74	30.53	23.74	0.34	6.23	Medium
5	180.44	8.15	67.36	22.14	0.37	5.00	Medium
6	236.80	8.37	109.32	28.29	0.46	4.65	Medium
7	120.38	6.53	98.68	18.43	0.82	3.50	Medium
8	130.14	6.86	55.40	18.97	0.43	4.64	Medium
9	180.13	6.33	65.42	28.46	0.36	3.45	Weak
10	64.24	2.14	18.15	30.02	0.28	4.97	Weak
11	82.46	4.20	21.71	19.63	0.26	2.56	Weak
12	89.33	3.33	27.56	26.83	0.31	3.32	Weak
13	120.69	5.41	30.22	22.31	0.25	4.34	Weak
14	195.53	7.10	42.60	27.54	0.22	5.55	Weak
15	115.50	3.52	11.62	32.81	0.10	2.70	No
16	150.93	5.42	34.21	27.85	0.23	2.80	No
17	178.96	4.37	18.80	40.95	0.11	1.46	No
18	78.84	4.75	13.50	16.60	0.17	3.30	No

The classification categories of rockburst tendency were strong (G_1), moderate (G_2), weak (G_3), and no rockburst (G_4). In other words, all of basic parameters were included in the three-dimensional matrix $G = (X_1, X_2, X_3)^T$, which formed the dataset of Bayesian model. These results were calculated as follows:

According to those selected training samples, the empirical probability is

$$p_1 = \frac{3}{18}, p_2 = \frac{5}{18}, p_3 = \frac{6}{18}, p_4 = \frac{4}{18}$$

The mean values of variable categories are

$$\mu_1(X_1^{(1)}, X_2^{(1)}, X_3^{(1)})^T = (16.73, 0.52, 6.89)$$
$$\mu_2(X_1^{(2)}, X_2^{(2)}, X_3^{(2)})^T = (22.31, 0.48, 4.80)$$
$$\mu_3(X_1^{(3)}, X_2^{(3)}, X_3^{(3)})^T = (25.80, 0.28, 4.03)$$
$$\mu_4(X_1^{(4)}, X_2^{(4)}, X_3^{(4)})^T = (29.55, 0.15, 2.57)$$

The matrix of mean values can be expressed as

$$\bar{X} = \begin{bmatrix} 16.73 & 22.31 & 25.80 & 29.55 \\ 0.52 & 0.48 & 0.28 & 0.15 \\ 6.89 & 4.80 & 4.03 & 2.57 \end{bmatrix}$$

The covariance matrixes of sample categories were

$$S_1^2 = \begin{bmatrix} 57.16 & -0.85 & 10.86 \\ -0.85 & 0.01 & -0.15 \\ 10.86 & -0.15 & 2.45 \end{bmatrix}$$

$$S_2^2 = \begin{bmatrix} 16.00 & -0.36 & 1.67 \\ -0.36 & 0.04 & -0.16 \\ 1.67 & -0.16 & 0.96 \end{bmatrix}$$

$$S_3^2 = \begin{bmatrix} 15.83 & 0.07 & 2.46 \\ 0.07 & 0.01 & -0.03 \\ 2.46 & -0.03 & 1.26 \end{bmatrix}$$

$$S_4^2 = \begin{bmatrix} 103.77 & -0.36 & -7.36 \\ -0.36 & 0.01 & 0.03 \\ -7.36 & 0.03 & 0.61 \end{bmatrix}$$

The covariance matrix of sample population was calculated as follow:

$$\Sigma = \begin{bmatrix} 40.63 & -0.27 & 1.33 \\ -0.27 & 0.01 & -0.07 \\ 1.33 & -0.07 & 1.20 \end{bmatrix}$$

while its inverse is

$$\Sigma^{-1} = \begin{bmatrix} 0.03 & 0.56 & 0.01 \\ 0.56 & 113.79 & 6.25 \\ 0.01 & 6.25 & 1.20 \end{bmatrix}$$

The discriminants for sample categories were obtained:

$$\begin{aligned} \omega_1(X_1, X_2, X_3) &= 0.78x_1 + 111.41x_2 + 11.58x_3 - 77.12 \\ \omega_2(X_1, X_2, X_3) &= 0.92x_1 + 97.77x_2 + 8.88x_3 - 56.56 \\ \omega_3(X_1, X_2, X_3) &= 0.90x_1 + 71.71x_2 + 6.68x_3 - 36.26 \\ \omega_4(X_1, X_2, X_3) &= 0.93x_1 + 49.87x_2 + 4.11x_3 - 24.28 \end{aligned}$$

Each group of sample data was brought into each discriminant function to obtain the corresponding posterior probability.

9.4.3 Verifying Accuracy of Bayesian Model

The research goal is to establish a more reliable model for predicting rockburst risk. Therefore, we introduced a multivariable Bayesian model using data of both lab and field. As shown in Table 9.2 and Fig. 9.8, the final classifications and posterior probabilities were calculated, demonstrating a high rate of accuracy.

Based on the original data, the results of predicting rockburst using the existing methods were compared. Significant differences were observed between the results of new method and the previous ones, even for a single sample, as shown in Table 9.2. With regard to predicting the actual rockburst grades, the accuracy rates of R_b, R_θ and W_{et} in isolation were 61, 72 and 56%, respectively. However, the multivariable Bayesian model was found to be significantly more reliable, with an accuracy rate of 94%. Only sample No. 11 experienced a relatively small error. These results were consistent with the notion that the Bayesian model could achieve more reliable predictions of rockburst risk.

In fact, there are many important factors that influence rockburst. Only a few factors were considered in the previous prediction methods. Rock brittleness index (R_b) was only considered the uniaxial compression strength and tensile strength; the stress of surrounding rockmass was not included in this model. Russenses's method (R_θ) deals with the principal stress of surrounding rockmass and uniaxial

Table 9.2 Posterior probability and return test

No.	Discriminants				Classified results	Backward possibility (%)
	W1	W2	W3	W4		
1	**75.72**	71.84	61.72	43.94	Strong	98.78
2	**59.05**	58.80	52.22	38.22	Strong	68.10
3	**85.83**	81.22	72.03	54.15	Strong	99.41
4	51.99	**54.18**	51.41	40.56	Medium	80.73
5	39.76	**44.67**	43.86	35.48	Medium	72.29
6	50.38	**55.85**	53.40	44.17	Medium	92.73
7	69.22	**71.60**	62.51	48.13	Medium	86.62
8	38.94	**43.68**	42.36	33.67	Medium	80.92
9	25.64	35.73	**38.46**	34.48	Weak	90.47
10	35.49	42.77	**44.24**	38.16	Weak	78.26
11	−2.72	9.95	17.41	**17.63**	No	65.21
12	16.77	27.73	**32.21**	29.70	Weak	88.05
13	18.56	26.95	**30.79**	26.80	Weak	94.91
14	33.05	63.96	**41.25**	35.01	Weak	94.54
15	−8.88	7.40	18.55	**22.35**	No	98.53
16	2.42	16.05	23.78	**24.43**	No	74.08
17	−16.36	4.31	17.91	**25.04**	No	99.95
18	−6.79	4.73	13.02	**13.26**	No	65.71

Note The Bold words are the maximum value of the discriminants, which indicates that the sample belongs to that classification.

Fig. 9.8 Rockburst in underground mining

compression strength. However, it did not account for the accumulated energy and rigidity of surrounding rockmass. Finally, Kidybinski's method (W_{et}) measured the rock capacity to store and release elastic energy, while many other factors were ignored. Obviously, there were limitations in the traditional methods for predicting rockbursts. Because rockburst was induced by multiple factors, considering a single factor alone inevitably leaded to imprecise results. Conversely, our model was benefitted from integrating the variables used in traditional methods, which could be input into the Bayesian model. In this chapter, R_b, R_θ and W_{et} were used as the critical factors in proposed model, plus the surrounding rockmass stress σ_1 and σ_θ, and rock strength σ_c and σ_t.

As shown in Table 9.3, the results were inconsistent for all samples using the previous methods, except for #1, 2, 8, and 16. Moreover, at least one method gave the incorrect rockburst grade for all samples besides #1, 2 and 8. On the other hand, the proposed model always returned the correct grade, except for sample 16.

The traditional methods were also limited in that they cannot differentiate the relative importance of different variables. In addition, it was not always reasonable to update the variables to coordinate the field data. A certain types of artificial intelligence, such as the neural network models, could consider many factors simultaneously; these methods did not address the empirical probabilities and posterior probabilities in their calculations. However, a Bayesian model could overcome these shortcomings to provide an ideal method for rockburst tendency prediction.

Because of limited availability of sample data, a self-validation process was implemented on the predictions from the new model. However, our results demonstrate that the new model is a significant improvement over existing methods, and can be implemented for predicting the reliable rockburst tendency.

Table 9.3 Comparison of predicted results

No.	Rock brittleness index (R_b)	Russenses's method (R_θ)	Kidybinski's method (W_{et})	Proposed model	Actual rockburst grades
1	***Strong***	***Strong***	***Strong***	***Strong***	***Strong***
2	***Strong***	***Strong***	***Strong***	***Strong***	***Strong***
3	Moderate	Moderate	Strong	Strong	Strong
4	Moderate	Moderate	Strong	Moderate	Moderate
5	Moderate	Moderate	Strong	Moderate	Moderate
6	Weak	Moderate	Moderate	Moderate	Moderate
7	Moderate	Strong	Moderate	Moderate	Moderate
8	***Moderate***	***Moderate***	***Moderate***	***Moderate***	***Moderate***
9	Weak	Moderate	Moderate	Weak	Weak
10	Weak	Weak	Moderate	Weak	Weak
11	Moderate	Weak	Weak	**None**	**Weak**
12	Moderate	Moderate	Weak	Weak	Weak
13	Moderate	Weak	Moderate	Weak	Weak
14	Weak	Weak	Strong	Weak	Weak
15	Weak	None	Weak	None	None
16	***Weak***	***Weak***	***Weak***	***None***	***None***
17	Weak	None	None	None	None
18	Moderate	None	Weak	None	None

Note The Bold and Italic words are the same as results using the different methods; The Bold words are different results by diverse methods.

9.5 Predicting Model of Rockburst Based on Fuzzy Matter Element Theory

9.5.1 Testing and Field Condition

9.5.1.1 Mining Conditions and Method

The 10# ore body in the Huize Lead–Zinc Mine is one of largest Pb–Zn deposits in China, and it is rich in poly metallic deposits including plumbum, zinc, and germanium. There are three ore bodies in the mine; they are 6#, 8# and 10#. The 6# ore body is located on upside the 8# ore body. The 6# and 8# ore body are close. However, the 10# ore body is located on the side of 8# ore body. The 10# ore body is the last one. In this chapter, the purpose of study plan is the predicting the rockburst for 10# ore body in this mine. The geological description was described in the document mining geometry and sequence in the volume (Wang et al. 2009; He and Wang 2010).

The ore grade of lead and zinc reaches 28%. The ore body consisted of sulfided and oxidized minerals. The surrounding rockmass is composed of four types of rock strata, which are lime stone (C_{3m}), hanging wall lime stone (C_{2w}), dolomite (C_{1b})

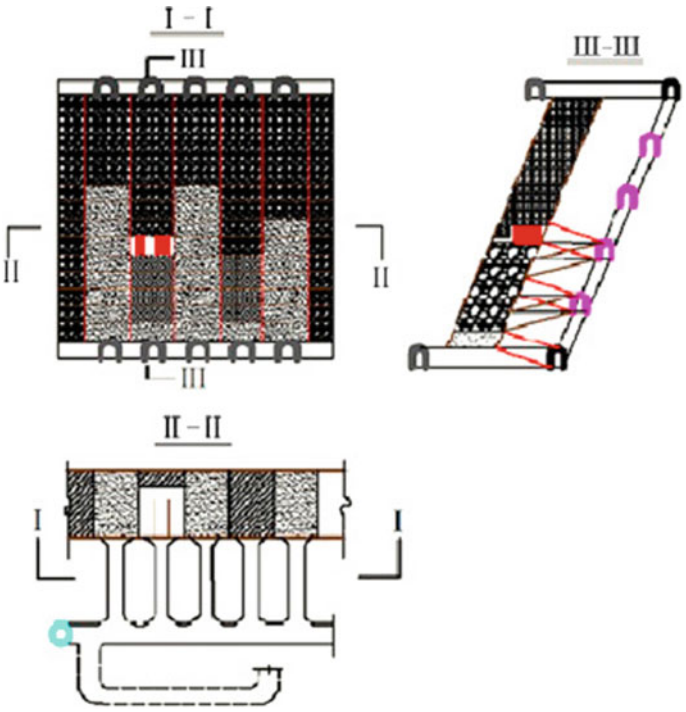

Fig. 9.9 Paste filling mining method of upward horizontal slice. With kind permission from "PERGAMON-ELSEVIER SCIENCE LTD": Fig. 1, Wang (2014). All rights reserved

and foot wall lime stone (C_{1d}). In 10# ore body, the working conditions are very complicated because of large depth, ample water, and fractured ore bodies. The deepest minable ore body is buried at a depth of more than 1500 m, which is now one of the deepest metal mines in China. This deep mining area is located in the eastern Yun-Gui plateaucany on area with very high virgin stress. With the increasing mining depths, the occurrence of rockburst increases and possesses greater safety threats to mining production. Adopting on the upward horizontal slice paste filling mining method in this mine, it was divided into two steps. As shown in Fig. 9.9. The mining sequence is from top to bottom. Nowadays, the goafs were immediately back filled with paste material. The length of 10# ore body strike and dip was 300 and 60 m, and the strike is N26 °E. The mine is mining the level 1331–1451 m level, level height was 60 m; sublevel height was 12 m, and layer height was 3 m. Stopes were vertically designed with the strike of ore body. Mining sequence is from 1451 m level to 1331 m level. The width of stope and pillar was 5 m or 6 m two schemes, the length was equal to the ore body thickness. Room was first stoped, and then room was filled with pasting. Pillar was stoped after the adjacent rooms were filled.

9.5.1.2 Laboratory Testing

In this testing, the physic-mechanic parameters of sulfide and oxidized ore body, disk lime stone (C_{3m}), hanging wall lime stone(C_{2w}), dolomite (C_{1b}) and foot wall lime stone(C_{1d}) samples were used testing, all tested samples were made and processed to standard cylindrical samples with 50 m mindiameter and 100 m from 1391 level. The elasticity modulus (E), Poisson's ratio (μ), uniaxial tensile strength (R_t) and uniaxial compressive strength (R_c) were conducted on rock mechanics testing system (MTS815), a computer controlled, servo hydraulic compression machine. The testing system was a Windows based platform with visual control operating software, which could record the current time, load, stress, displacement, strain value, load-displacement curve and stress-strain curve, etc. The equal-displacement loading was selected as the control mode in the test. The specimen was loaded at a constant loading rate of 2×10^{-3} mm/s until the specimen fails. R_t was calculated using the Brazil testing method, while V_p and V_{pm} were obtained with the CE-9201 rock engineering testing machine, where V_p was the longitudinal wave velocity of sample, and V_{pm} was the longitudinal wave velocity of rockmass. The tested physi-mechanical parameters of sulfide and oxidized ore body, disk lime stone (C_{3m}), hanging wall lime stone (C_{2w}), dolomite (C_{1b}) and foot wall lime stone (C_{1d}) samples were shown in Table 9.4.

9.5.1.3 Stress Estimation

The stress relief method was used to estimate the stress in 1391 level of ore body 10#. Two measurements position design were showed in Fig. 9.10. In the field, the hollow inclusion measurement is one of stress relief methods; the triaxial stress probes (Institute of geology and geophysics, Chinese academy of science, Beijing, China) can obtained the triaxial stress status at the point in single borehole. The measurement procedures are as follows (Amadei 1983; Amadei and Stephansson 1997).

Table 9.4 Physi-mechanical parameters tested results for rock stratums

Samples	ρ (g/cm^3)	E (GPa)	μ	R_c (MPa)	R_t (MPa)	V_{pr} (m/s)	V_{pm} (m/s)
Sulfide ores	4.09	15.09	0.25	86.24	3.01	4174	3757
Oxidized	4.57	14.62	0.25	85.88	4.12	4280	3890
C_{2w}	2.8	17.8	0.24	74.68	6.08	5102	4151
C_{1b}	2.78	17.17	0.26	68.66	3.07	5016	4568
C_{1d}	2.71	16.35	0.27	104.11	4.44	4955	4387
C_{3m}	2.53	8.29	0.28	20.13	1.39	3063	2580

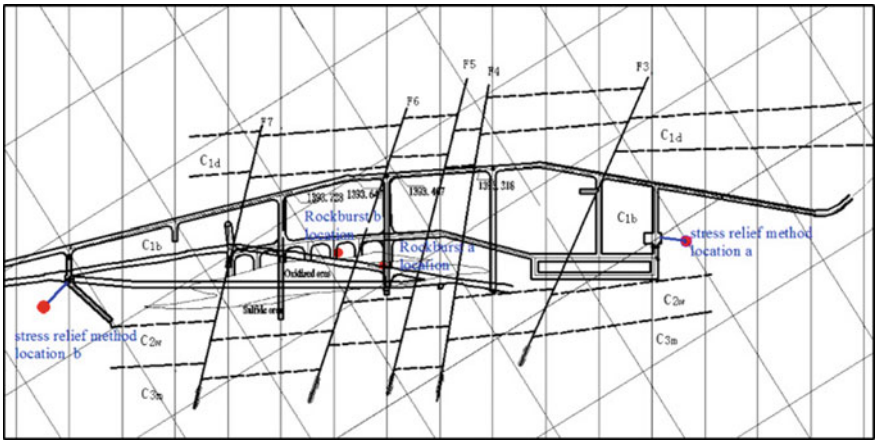

Fig. 9.10 Rockbursts cases and stress relief method positions in 1391 level. With kind permission from "PERGAMON-ELSEVIER SCIENCE LTD": Fig. 2, Wang et al. (2015). All rights reserved

Table 9.5 The measured results of stress in 1391 level of 10# ore-body

Excavated surrounding rockmass	σ_1 (MPa)	Azimuth angle	Drilling depth (m)	Remarks
C_{1b}	32.66	206.4	17.5	Stress relief method
	31.73	204.4	17.5	

With kind permission from "PERGAMON-ELSEVIER SCIENCE LTD": Table 2, Wang et al. (2015). All rights reserved

Firstly, the diameter 130 mm bore was drilled at the measured point, the depth of borehole was approximate 18 m. Secondly, the diameter 36 mm pilot hole was drilled in the centre of diameter 130 mm bore; the depth of hole was approximate 36 mm. Thirdly, the measurement probe was installed in this hole, the initial value was obtained. Fourthly, after curing cement, releasing the stress, the diameter 36 mm of over coring bore was drilled, the injected water pressed the strain gauges onto the walls of pilot hole. The data were obtained after every drilled 30 mm, the rock core was drawn, over coring was terminated. Fifthly, the procedures 2–4 were recovered, the acquired data could be verified the previous ones. In this research, the calculated major principal stress was selected the average value, namely, 32.2 MPa.

The results showed that the major principal stress magnitude was the similar as the gravity stress field. However, the azimuth angle of major principal stress was approximately parallel the trend of ore body (N26 E), as shown in Table 9.5.

9.5.2 Predicting Rockburst Tendency

Rockburst tendency is used to confirm the qualitative or quantitative induced possibility of rockburst by the tested method. It is usually divided into four strength grades, namely, no rockburst, weak rockburst, medium rockburst and strong rockburst. The traditional test methods are Barton method, rock brittleness, impact tendency energy and rock integrity. As shown in Table 9.5, it explains the scope of data in the four strength grades using traditional predicting methods. The columns show the data scope of one predicting method bases four strength grades, and the rows show the data scope of strength grades bases the different predicting methods. These terms are related to different parameters with different predicting method, for example, the rock brittleness method is shown as the uniaxial compressive strength and uniaxial tensile strength. However, Barton method is shown as the uniaxial compressive strength and the maximum principal stress. As shown in Table 9.5, the strength grades of rockburst were divided according to the different method.

9.5.2.1 Predicting Rockburst Tendency Using Traditional Method

Several rockburst tendency prediction methods were usually used in practice, the strength grades of methods were shown in Table 8.2. They considered many factors including geostress, rock brittleness, rock integrity and other aspects. These methods were given as follows:

(1) Barton's method (Barton et al. 1974). Here in after referred to as α. In general, the elastic strain energy of hard rock was higher than that of soft rock in the high stress zone. Rock strength stress ratio $\alpha = R_c/\sigma_1$ was generally used to determine the rockburst tendency, where R_c was the UCS, and σ_1 was the major principal stress.

(2) Rock brittleness (Tan et al. 1991). Here in after referred to as B. The UCS R_c and UTS R_t were the main factors affecting the rock brittleness. The brittleness coefficient $B = R_c/R_t$ could be used to predict the possibility of rockburst.

(3) Impact tendency energy (Singh 1988). Here in after referred to as W_{CF}, which was determined by the load-deformation curve of rock. Given that F_1 was the area before the peak and F_2 was the area after the peak, the impact energy index was calculated as $W_{CF} = F_1/F_2$. The larger W_{CF} value meant the more likely rockburst would occur.

(4) Rock integrity (Hou and Wang 1989). Here in referred to as K_V. In the same initial stress conditions, the intact, hard, compact and brittle rock could produce enough energy to cause the local broken rock, to suddenly release and cause rockburst at a certain stress level, as shown in Eq. (9.1).

$$K_V = \frac{V_{pm}^2}{V_{pr}^2} \tag{9.1}$$

where K_V is the rock integrity coefficient; V_{pm} is the rockmass elastic wave speed, m/s; V_{pr} is the rock elastic wave speed, m/s.

This grade classification was generally obtained based on the range of predicted value. Each predicting methods of rockburst tendency were divided into four strength grades, and the specific grade situation was shown in Table 9.3.

9.5.2.2 Predicting Rockburst Tendency Using the Proposed Model

Fuzzy matter-element theory was applied to evaluate multi-index incompatible problem. It is used to solve to the problem with the method of visualization. Fuzzy matter-element model of rockburst tendency was established (Wang et al. 2015), and the steps of predicting rockburst tendency were shown as follows.

(1) Establishing fuzzy matter-element

1. According to the strength grades of rockburst tendency (as shown in Table 9.3), the obtained physi-mechanical parameters and stress (as shown in Tables 9.2 and 9.3) were used to establish the fuzzy matter-element matrix for rockburst evaluation.

$$R_{(4,10)} = \begin{bmatrix} & \textit{Sulphide ores} & \textit{Oxidized ores} & C_{2w} & C_{1b} & C_{1d} & C_{3m} \\ B & 28.680 & 20.825 & 12.291 & 22.354 & 23.433 & 14.490 \\ R_c/\sigma_1 & 2.678 & 2.667 & 2.319 & 2.132 & 3.233 & 0.625 \\ W_{CF} & 1.210 & 2.210 & 2.160 & 1.120 & 0.910 & 1.210 \\ K_V & 0.810 & 0.870 & 0.664 & 0.833 & 0.784 & 0.711 \end{bmatrix}$$

No rockburst	*Weak rockburst*	*Medium rockburst*	*Strong rockburst*
>40.000	$26.700-40.000$	$14.500-26.700$	<14.500
>10.000	$5.000-10.000$	$2.500-5.000$	<2.500
<1.000	$1.000-2.000$	$2.000-3.000$	>3.000
<0.500	$0.500-0.600$	$0.500-0.750$	>0.750

2. According to the preferable membership grade principle, the model was given in the larger the more optimal principles in the intensity of rockburst in creases with the decreased of R_c/σ_1 and B. On the contrary, as the in tensity of rockburst increased with the rise of W_{CF} and K_V, the model adopted the smaller them ore optimal principle. Namely, $\mu_{ij} = X_{ij}\min/X_{ij}$. The composite fuzzy matter-element matrix was established as follow:

Table 9.6 Predicting rockburst tendency grades using traditional method

Strength grade	B	α	W_{CF}	K_V
No rockburst	>40.0	>10.0	<1	<0.50
Weak rockburst	26.7–40.0	5.0–10.0	1–2	0.50–0.60
Medium rockburst	14.5–26.7	2.5–5.0	2–3	0.60–0.75
Strong rockburst	<14.5	<2.5	>3	0.75–1.00

With kind permission from "PERGAMON-ELSEVIER SCIENCE LTD": Table 3, Wang et al. (2015). All rights reserved

$$R_{(4,10)} = \begin{bmatrix} & \textit{Sulphide ores} & \textit{Oxidized ores} & C_{2w} & C_{1b} & C_{1d} & C_{3m} \\ B & 0.717 & 0.521 & 0.307 & 0.559 & 0.586 & 0.362 \\ R_c/\sigma_1 & 0.268 & 0.267 & 0.232 & 0.213 & 0.323 & 0.063 \\ W_{CF} & 0.752 & 0.412 & 0.421 & 0.813 & 1.000 & 0.752 \\ K_V & 0.617 & 0.605 & 0.753 & 0.600 & 0.638 & 0.703 \end{bmatrix}$$

$$\begin{bmatrix} \textit{No rockburst} & \textit{Weak rockburst} & \textit{Medium rockburst} & \textit{Strong rockburst} \\ > 1.000 & 0.668 - 1.000 & 0.363 - 0.668 & < 0.363 \\ > 1.000 & 0.500 - 1.000 & 0.250 - 0.500 & < 0.250 \\ < 0.910 & 0.455 - 0.910 & 0.303 - 0.455 & > 0.303 \\ < 1.000 & 0.833 - 1.000 & 0.667 - 0.833 & > 0.667 \end{bmatrix}$$

3. According to the composite fuzzy matter-element matrix, the preferable membership grade of index extract value 1 for predicting closer to reality, the different square were composite fuzzy elements were established (Table 9.6):

$$R_{(4,10)} = \begin{bmatrix} & \textit{Sulphide ores} & \textit{Oxidized ores} & C_{2w} & C_{1b} & C_{1d} & C_{3m} \\ B & 0.080 & 0.230 & 0.480 & 0.195 & 0.172 & 0.407 \\ R_c/\sigma_1 & 0.536 & 0.538 & 0.590 & 0.619 & 0.458 & 0.879 \\ W_{CF} & 0.062 & 0.346 & 0.619 & 0.035 & 0.000 & 0.062 \\ K_V & 0.147 & 0.156 & 0.061 & 0.160 & 0.131 & 0.088 \end{bmatrix}$$

$$\begin{bmatrix} \textit{No rockburst} & \textit{Weak rockburst} & \textit{Medium rockburst} & \textit{Strong rockburst} \\ 0.000 & 0.000 - 0.111 & 0.111 - 0.406 & > 0.406 \\ 0.000 & 0.000 - 0.250 & 0.250 - 0.563 & > 0.563 \\ 0.000 & 0.008 - 0.297 & 0.297 - 0.485 & > 0.485 \\ 0.000 & 0.000 - 0.028 & 0.028 - 0.111 & > 0.111 \end{bmatrix}$$

(2) Calculating the weight coefficient using the entropy method
The evaluation matrix was normalized and the entropy H_i and w_i were calculated according to Eqs. (8.12)–(8.16).

$$B_{ij} = \begin{bmatrix} & \textit{Sulphide ores} & \textit{Oxidized ores} & C_{2w} & C_{1b} & C_{1d} & C_{3m} \\ B & 0.000 & 0.374 & 1.000 & 0.286 & 0.229 & 0.817 \\ R_c/\sigma_1 & 0.186 & 0.190 & 0.314 & 0.383 & 0.000 & 1.000 \\ W_{CF} & 0.178 & 1.000 & 0.968 & 0.102 & 0.000 & 0.178 \\ K_V & 0.865 & 0.965 & 0.000 & 1.000 & 0.711 & 0.274 \end{bmatrix}$$

$$H_i = [0.984 \quad 0.986 \quad 0.977 \quad 0.984]^T \quad (\mathrm{i} = 1, 2, 3, 4)$$
$$w_i = [0.228 \quad 0.209 \quad 0.338 \quad 0.226]^T \quad (\mathrm{i} = 1, 2, 3, 4)$$

(3) The closeness degree calculation
The composite fuzzy matter-element for closeness degree was established by Eq. (8.16):

$$R_{\rho H} = \begin{bmatrix} \textit{Sulphide ores} & \textit{Oxidized ores} & C_{2w} & C_{1b} & C_{1d} & C_{3m} \\ 0.571 & 0.437 & 0.401 & 0.529 & 0.595 & 0.437 \\ \textit{No rockburst} & \textit{Weak rockburst} & \textit{Medium rockburst} & & \textit{Strong rockburst} & \\ > 0.904 & 0.571 - 0.948 & 0.368 - 0.571 & & < 0.368 & \end{bmatrix}$$

9.5.3 *Predicting Model of Fuzzy Matter-Element Theory*

9.5.3.1 Comparison and Analysis of Predicting Model

The results of rockburst tendency for surrounding rockmass and ore body were calculated by these four predicting methods in the 10# ore body. The calculation results were shown in Table 9.7. Based on the calculations of closeness degree, the evaluation of rockburst tendency for the surrounding rockmass in 10# ore body was obtained using fuzzy matter-element evaluation model, as shown in Table 9.8. There results showed that C_{1d} had weak rockburst tendency. The sulfide ores, oxidized ores, C_{2w}, C_{1b} and C_{3m} had medium rockburst tendency. There results were compared with those calculations obtained.

As shown in Table 9.8. It was concluded that the rockmass in the 1331–1451 levels of 10# ore-body had the possibility of medium rockburst in sulfide ores, oxide minerals, C_{2w}, C_{1b} and C_{3m}, and the weak rockburst maybe be occurred in the C_{1d}.

Table 9.7 Results of each rockburst predicting methods in 10# ore body

Ore and rockmass	B	α	W_{CF}	K_V
Sulfide ores	28.680	2.678	1.210	0.810
Oxidized ores	20.825	2.667	2.210	0.827
C_{2w}	12.291	2.319	2.160	0.664
C_{1b}	22.354	2.132	1.120	0.833
C_{1d}	23.433	3.233	0.910	0.784
C_{3m}	14.490	0.625	1.210	0.711

Table 9.8 Comparison of predicting results

Ore and rockmass	B	α	W_{CF}	K_V	Fuzzy Matter element model
Sulfide ores	Weak	Medium	Weak	Strong	Medium
Oxidized ores	Medium	Medium	Medium	Strong	Medium
C_{2w}	Strong	Strong	Medium	Medium	Medium
C_{1b}	Medium	Strong	Weak	Strong	Medium
C_{1d}	Medium	Medium	No	Strong	Weak
C_{3m}	Strong	Strong	Weak	Medium	Medium

9.5.3.2 Data Analysis and Discussions

In 10# ore body, rockburst occurred at the drift, 5 panel, 1391 m level on Oct 11st, 2012 (Fig. 9.11a). It was approximately 100 t in the C_{1b} rock strata. The other rockburst occurred at the drift, 7 panel, 1391 m level on Nov 28th, 2013 (Fig. 9.11b). It was approximately 50 t in the C_{1b} rock strata.

The mining engineering only excavated in the C_{1b} stratum, sulfide ore sand oxidized ores. As shown in Fig. 9.11. The other stratums indiced of predicting model were obtained by the borehole in the laboratory and field. So the case rockbursts could only be occurred in the C_{1b}, sulfide ore sand oxidized ores. However, the sulfide ore sand oxidized ores were mined by the immediate paste backfilling, the ores stratums stress could be controlled by the filling body, and it might be not occur the rockbursts.

The grade for two rockburst tendency of C_{1b} was different according to different evaluation methods. It was strong with Barton method (α method) and rock integrity method (K_V method), medium with fuzzy matter-element model and rock brittleness method (B method), weak with impact tendency energy method (W_{CF} method). To acquire the compared different results, the research concluded that these results were related with the considered factors of different method. As

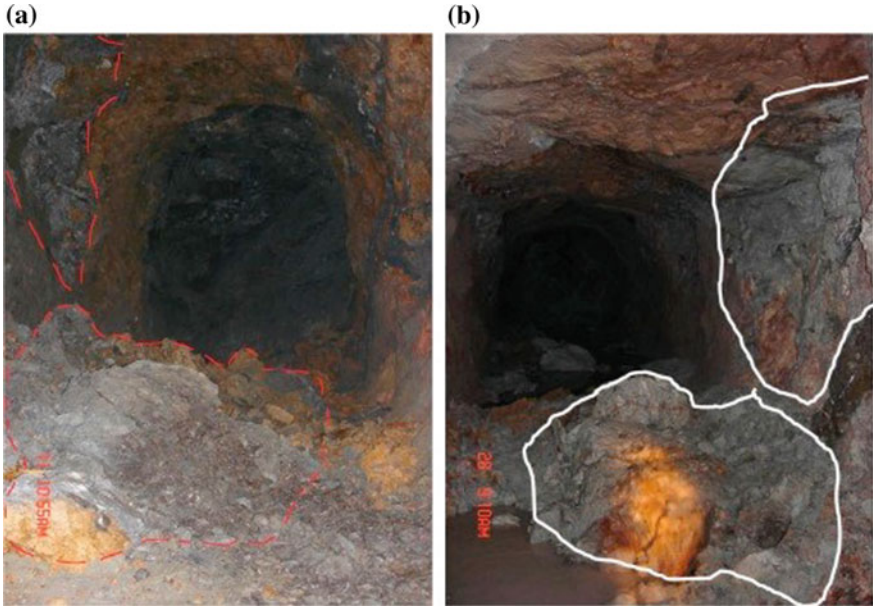

Fig. 9.11 Rockbursts on site. With kind permission from "PERGAMON-ELSEVIER SCIENCE LTD": Fig. 3, Wang et al. (2015). All rights reserved

follow, Barton method only considered the UCS and the major principal stress, but the brittleness and integrity of rock were not included in the model. However, 10# ore body and other rock stratums were not particularly intact, the predicting result of Barton method might be slightly higher than the actual value, its predicting result was strong rockburst grade; Rock brittleness method didn't contain the major principal stress, which was the base factor for the rockburst tendency. It was important that the stress caused the accumulated energy of rockmass, its predicting result was medium rockburst grade, and this result was the same as the fuzzy matter-element model. However, in other predicting result of rock brittleness method, they might be away from the true value because of lacking the most important factor in stress; Impact tendency energy method only considered the before and after peak value, rock brittleness was only one of factors of rockburst tendency. However, the parameters, such as the stress and the intact degree, were important factors in the predicting result. In this research, we could find that the curve was mitigated. So the predicting of impact tendency energy method was quiet low; Rock integrity method didn't include the major principal stress, rock brittleness and the impact tendency energy, which were the base factors of energy accumulation. That is to say, these traditional methods exited the limitations for rockburst tendency. However, fuzzy matter-element model were obtained using all factors of traditional method, the predicting result using fuzzy matter-element method for rockburst was medium in 1391 level of C_{1b} rock strata in 10# ore body,

as shown in Table 9.8. For exposing rockmass and ore body in this mine depth, the case results showed that fuzzy matter-element predicting was right. Because no other rock stratums exposed, such as C_{2w}, C_{1b} and C_{3m}, we only obtained the predicting results from C_{1b}, so the proposed model needs further validation. However, the two cases showed that the proposed model could predict rockburst in a reliable mode; this is a meaningful discovery for predicting rockburst tendency.

9.6 Conclusion

A large number of AE information before and during rockburst was obtained using AE experiments of rock under cyclic load/unload. Through CT scanning technology, we reconstructed the fissured rock in three-dimensions and built the cracks growth factor model. Furthermore, the predicting key points of precursor information were obtained by analyzing the nonlinear dynamics evolution pattern of rock cracks and fissured rock mass.

Many models and cases of precursor information prediction of rockburst have been described in this chapter, such as Bayesian model, Fuzzy matter-element model, TDF identification, TM identification, information entropy and b value, load/unload response ratio, infrared radiation, CAV and MS rate, spatial-temporal-energy evolution model of rock failure, etc. These cases verified that the proposed model and theory could predict rockburst in a reliable mode. This is a meaningful discovery for predicting rockburst.

It was worth mentioning that we used a Bayesian multi-parameter model to predict rockburst tendency by improving upon other traditional prediction methods. Cases results show that the proposed predicting models were more reliable than those traditional methods. The results demonstrated that the multivariable Bayesian model was highly accurate in predicting rockburst tendency. We recommend that Bayesian models to predict rockburst in field.

In addition, compared with traditional methods, fuzzy matter-element method was verified based on the rockburst in field. The results showed that the fuzzy matter-element was very prominent for the predicting rockburst intensity. Obtaining more accurate results of fuzzy matter-element model, we proposed in put many parameters. This may improve predicting quality.

Finally, we recommend the proposed predicting methods of rockburst for field cases.

References

Amadei B (1983) Number of bore holes to measure the state of stress in situ by overcoring. In: The 24th US Symposium on Rock Mechanics (USRMS). College Station, Assoc Eng Geol Publ, pp 87–98

Amadei B, Stephansson O (1997) Rock stress and its measurement. Chapman&Hall, London

Barton NR, Lien R, Lunde J (1974) Engineering classification of rockmasses for the design of tunnel support. Rock Mech 6:189–239

Cheng Y, Jiang F, Cheng J (2006) Preliminary study on microseismic monitoring of mine tremor induced by key strata movement. J Coal Ind 31(3):273–275

He SL, Wang CL (2010) Analysis of influencing factors of rockburst in deep mining in Huize lead–zinc mine. Miner Eng Res 25:21–23 (in Chinese)

Hou FL, Wang MQ (1989) Criterion and prevention measures on rockburst in circular tunnel. In: Proceedings of the 2nd national rock mechanics and engineering (Chinese Rock Mech Eng). Knowledge Press, Beijing

Li S, Yin X, Deng W (2005) The research of Fankou mine multi-channel microseismic monitoring system and its application. J Rock Mech Eng 24(12):2058–2059

Liu J (2008) A new rock mass stability monitoring system based on AE and microseismic technology and its application. Nonferrous Metal Mine Sect 60(4):32–35

Singh SP (1988) Burst energy release index. Rock Mech and Rock Eng 21(2):149–155

Tan Y, Sun GZ, Guo ZH (1991) A composite index K(rb) criterion for the ejection characteristics of the burst rock. Chin J Geol 2:193–200

Wang CL (2013) Identification and early warning method for rock mass instability. Disaster Adv 6 (12):101–105

Wang CL (2014) Identification of early-warning key point for rockmass instability using acoustic emission/microseismic activity monitoring. Int J Rock Mech Min Sci 71:171–175

Wang CL, Wu AX, Liu XH (2009) Mechanisms of microseismic events occurred in deep heard-rock mine of China. In: Proceedings seventh international symposium on rockburst and seismicity in mines, Liaoning Dalian

Wang CL, Wu AX, Lu H, Bao TC, Liu XH (2015) Predicting rockburst tendency based on fuzzy matter–element model. Int J Rock Mech Min Sci 75:224–232